Nanoscale

Accepted Manuscript

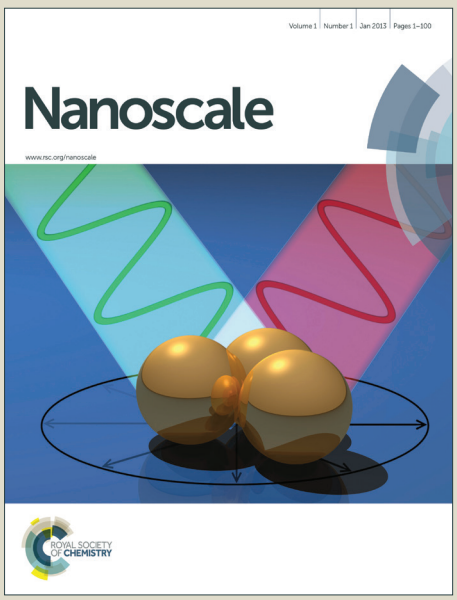

ROYAL SOCIETY OF CHEMISTRY

www.rsc.org/nanoscale

Nanoscale

PAPER

Catalytic activity for oxygen reduction reaction on platinum-based core-shell nanoparticles: all-electron density functional theory

Received 00th January 20xx,
Accepted 00th January 20xx

DOI: 10.1039/x0xx00000x

www.rsc.org/

Jungho Shin[a,b], Jung-Hae Choi[a], Pil-Ryung Cha[c], Seong Keun Kim[a], Inho Kim[a], Seung-Cheol Lee*[a], and Doo Seok Jeong*[a]

Pt nanoparticles (NPs) in a proton exchange membrane fuel cell as a catalyst for the oxygen reduction reaction (ORR) fair overbind oxygen and/or hydroxyl to their surfaces, causing to large overpotential, and thus low catalytic activity. Realizing Pt-based core-shell NPs (CSNPs) is perhaps a workaround for weak binding of oxygen and/or hydroxyl without shortage of sufficient oxygen molecule dissociation on the surface. Towards this end, we theoretically examined catalytic activity of NPs by means of density functional theory; each consists of one of 12 different 3*d*–5*d* transition metal cores (groups 8–11) and a Pt shell. The calculation results evidently suggest the enhancement of catalytic activity of CSNPs, in particular, with 3*d* transition metal cores in use. The revealed trends in activity change upon core metal were discussed regarding thermodynamic and electronic structural aspects of the NPs in comparison with the general *d*-band model. The disparity between the CSNP and the corresponding bilayer catalyst – so called size effect – was remarkable so that it perhaps opens up the possibility of size determined catalytic activity. Finally, the overpotential for all CSNPs was evaluated in an attempt to choose promising combinations of CSNP materials.

Introduction

As an alternative to mainstream alkaline fuel cells, proton exchange membrane fuel cells (PEMFCs) are a subject of great interest given several advantages such as low operational temperature and pressure, and structural simplicity favorable for scaling down. Alongside these advantages, what this technology is distinguishable is such that the PEMFC technology is environment-friendly. The PEMFC technology with promise has been investigated for several decades and, for the time being, it is being close to mass-production albeit still challenging. One of the challenges lies in reconciling the performance with the cost; the cost should not outweigh the aforementioned benefits of the PEMFC technology. In this regard, making use of Pt catalysts[1] for the oxygen reduction reaction (ORR) at the cathode is required to be reconsidered and, in fact, attempts to replace Pt entirely or partly by inexpensive catalytic materials are ongoing.[2-7] Given that the overpotential for the ORR directly determines the performance, i.e. open-circuit voltage, an alternative to film-type Pt catalysts should be chosen carefully so as to avoid sacrificing the performance to a great extent. In this regard, employing Pt nanoparticles (NPs) is seemingly an interesting approach in light of their large surface area per mass, which perhaps maximize the catalytic effect of Pt.

However, compared with a preferentially (111)-oriented Pt film, Pt NPs appear to overbind the two types of adsorbates (O and OH), being directly involved in the operation, to their surfaces. The catalytic activity of the NPs therefore decreases (the overpotential for the ORR increases), and thus so does the open-circuit voltage.[1] In addition, overbinding adsorbates leads to the shortage of active catalytic sites given the lack of desorption of adsorbates.[10-13] A possible workaround solution these problems without giving up the advantage of Pt NPs may be to utilize a core-shell-type NP (CSNP) in which the core is replaced by other metal than Pt but the same Pt shell. The metal underneath the Pt surface evokes a change in the *d*-band center of the surficial Pt layer, by and large, due to the ligand effect[14,15] and the strain effect.[16] Given that the surface binding, i.e. adsorption, energy of the adsorbates appears largely determined by *d*-band center position[17], the core kind may significantly modify the adsorption energy, bringing the energy under control.[3,18,19]

Experimental attempts to identify the ORR catalytic activity for synthesize CSNPs of Pt shells (core@Pt) have been made.[6,7,20-22] Alongside experimental identification, CSNPs have also been subject to density functional theory (DFT) calculations[3,19-21,23]; as a consequence, the theoretical catalytic activities of several core-shell combinations are available, albeit limited, in particular, for core@Pt CSNPs.[3,19] Notably, CSNPs under theoretical investigation are often put in the framework of bilayer models, i.e. slab models[2,15,20,21,24,25] for calculations

[a] Center for Electronic Materials, Korea Institute of Science and Technology, Hwarang-ro 14-gil 5, Seongbuk-gu, Seoul 136-791, Republic of Korea. E-mail: leesc@kist.re.kr, dsjeong@kist.re.kr; Tel: +82-2-958-6781, +82-2-958-5490; Fax: +82-2-958-6658, +82-2-958-5509
[b] Center for Advanced Materials Technology, Kookmin University, Jeongneung-ro 77, Seongbuk-gu, Seoul 136-702, Republic of Korea
[c] School of Advanced Materials Engineering, Kookmin University, Jeongneung-ro 77, Seongbuk-gu, Seoul 136-702, Republic of Korea

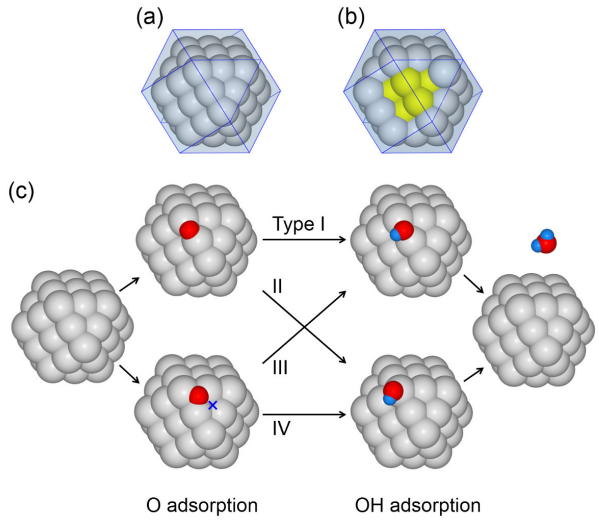

Fig. 1 Schematics of (a) an NP and (b) an NP with a highlighted core. The triangular and the square plane in (a) and (b) denote a (111) and a (100) facet, respectively. (c) Four possible ORR pathways (Type I – IV) depending upon active sites for the reaction intermediates – O and OH – for the ORR. A red and a blue atom illustrate O and H, respectively. Both Type I and II involve the common *O site (bridge site) but different *OH sites (bridge for Type I and atop for Type II). Type III and IV involve the common *O site (hollow site) but different *OH sites (bridge for Type III and atop for Type IV). The blue-coloured mark × points to a hollow site that cannot stabilize *O because of the very low binding energy.

simplicity. However, the same as results from such slab models may not hold true for CSNP model systems, in particular, when it comes to a CSNP with a few nanometer diameter. In this case, the non-negligible portion of irregular adsorption sites, i.e. edges and vertices, perhaps assigns a distinguishable catalytic activity to the CSNP. In other words, the slab model approximately features a larger CSNP, in which facets – rather than irregular sites such as vertices and edges – predominantly provide the adsorbates with adsorption sites. Evaluating catalytic activity for CSNP model systems of rich core-shell combinations is therefore of great importance in underpinning the previous slab approximation, modifying the approximation if necessary, enriching a database of CSNP's activity, and eventually acquiring the optimum core-shell combination(s). Regarding the latter, a further systematic fine tuning of catalysts, including core-shell materials and CSNP dimension, is required following the previous seminal works.[1,26,27] Towards this end, we estimated the catalytic activity for core@Pt CSNPs with 11 different core metals, $3d$ – $5d$ transition metals in groups 8 – 11, by evaluating the adsorption energies of O and OH adsorbates on their surfaces.

An attempt to find a trend in the activity change upon the core kind was then made. The core metal-depending adsorption energies were understood in terms of a change in the *d*-band center position of the surface Pt layer. To highlight the contrast between the core-shell and the slab model, the adsorption energies of O and OH for several core-shell combinations were compared with the corresponding slab models, providing a noticeable difference for some cases. Hereafter, 'catalyst' means 'catalyst for the ORR' unless otherwise stated.

Computational details

Both CSNPs and slabs in the calculations were fully relaxed following their initial atomic configurations. The relaxed lattice parameter of face-centered cubic (FCC) Pt was calculated to be 3.97 Å – in good agreement with the experimental value (ca. 3.92 Å) with an error range of approximately +1.3 %. First, a Pt_{55} NP of 1 nm in diameter was assumed to be of cuboctahedral (COh) morphology as shown in Figure 1a. In this structure, the NP consists of one Pt atom being placed at the center of the NP and two folded shells covering the centered atom. The outermost shell is a surface monolayer of 42 atoms and (100) and (111) facets are exposed (Figure 1a). The inner shell is made of 12 atoms. To form a CSNP the inner 13 atoms – including 12 atoms in the inner shell and the one centered atom – were replaced with another element that serves as a core. A schematic of such a core is illustrated in Figure 1b. 11 different core metals were examined: $3d$ – $5d$ transition metal elements ranging from group 8 to 11.

Four different slab models – Pt(100), Pt(111), Pt/Au(111), and Pt/Cu(111) – were examined for control experiments. The Pt(100) and Pt(111) slabs were formed with the aforementioned lattice parameter of bulk Pt (3.97 Å). Likewise, the FCC Au(111) and Cu(111) slabs were introduced with the relaxed lattice parameter of bulk structure – 4.16 and 3.63 Å, respectively, which are in good agreement with the experimental values (4.08 and 3.61 Å, respectively). The topmost layer of each slab was replaced with Pt for a bilayer catalyst. For all slab models, a $p(3\times3)$ supercell was under test and each slab was of four layers (ca. 0.62 – 0.71 nm thick). The slabs were also fully relaxed with the two bottom layers being fixed at the initial lattice parameter.

Regarding thermodynamic quantities, the adsorption energy of an adsorbate (ΔE_{ads} where $ads \in \{O, OH\}$) was calculated using the following equation:

$$\Delta E_{ads} = E_{ads/cat} - (E_{cat} - E_{ads}), \quad (1)$$

where $E_{ads/cat}$ is the total energy of the catalyst with the adsorbate. E_{subs} and E_{ads} denote the energies of the catalyst and the adsorbate, respectively, without interaction. The free energy change upon the reaction (ΔG) was obtained from the following equation:

$$\Delta G = \Delta E + \Delta ZPE - T\Delta S, \quad (2)$$

where ΔE, ΔZPE, T, and ΔS mean the energy change, the difference in zero point energy, the temperature, and the entropy change, respectively. ΔZPE and ΔS were obtained from previous reports.[1,28-30] The effect of external bias on the reaction was implemented by a shift in the electrostatic energy of an electron: –eU, where U denotes the electrode potential.[1]

Table 1 O and OH adsorption energies on possible sites – bridge and hollow sites for *O and atop and bridge sites for *OH – for each CSNP. The preferred pathway of an ORR for each CSNP is accordingly written. The more energenetically stable site is indicated by gray. The light gray denotes a disparity below 0.05 eV so that none of two is distinguishably favourable.

CSNP	*O (eV)		*OH (eV)		Type
	Bridge	Hollow	Atop	Bridge	
$Fe_{13}@Pt_{42}$	-4.62	-4.62	-3.14	-3.11	I, II, III, IV
$Co_{13}@Pt_{42}$	-4.80	-4.54	-3.00	-2.98	I, II
$Ni_{13}@Pt_{42}$	-4.88	-4.56	-3.04	-3.10	I
$Cu_{13}@Pt_{42}$	-4.90	-4.54	-2.97	-3.08	I
$Ru_{13}@Pt_{42}$	-4.73	-4.66	-3.12	-3.10	I, II
$Rh_{13}@Pt_{42}$	-4.85	-4.67	-3.29	-3.22	II
$Pd_{13}@Pt_{42}$	-4.96	-4.77	-3.34	-3.28	II
$Ag_{13}@Pt_{42}$	-5.03	-5.06	-3.01	-3.26	I, III
$Os_{13}@Pt_{42}$	-4.78	-4.72	-3.11	-3.14	I, II
$Ir_{13}@Pt_{42}$	-4.88	-4.67	-3.36	-3.32	I, II
Pt_{55}	-4.99	-4.73	-3.44	-3.32	II
$Au_{13}@Pt_{42}$	-5.09	-5.09	-3.21	-3.33	I, III

All calculations engaged the Perdew-Burke-Ernzerhof (PBE96)[31] exchange-correlation functional alongside the FHI-aims code[32,33], providing a numeric atomic orbital (NAO) basis set. The NAO basis set is considered suitable for zero dimensional systems such as NPs.[32] The *light* default basis set was employed for all considered atoms. This circumstance encompasses the minimal basis with added functions of partial tier 1 (*s, p, d, f*) for transition metals, which is often referred to as double numeric plus polarization. In addition, the scalar relativistic effect using the zero-order regular approximation[32,34] was take into consideration, which is likely required for heavy atoms such as all the transition metals. For slab models, the Brillouin zone was sampled with a 6 × 6 × 1 *k*-point grid for (100) and (111) surfaces, based on Monkhorst-Pack grids and gamma-centered. The Hellmann-Feynman forces[35,36] were employed for atomic relaxation until the residual force components fell below 0.01 eV/Å. However, when the NP's morphology was transformed to the other morphology (e.g. icosahedron) during the relaxation, the residual force components were adjusted below 0.05 eV/Å to maintain the COh morphology. Such force adjustment was required for $Co_{13}@Pt_{42}$, $Fe_{13}@Pt_{42}$, $Ni_{13}@Pt_{42}$ and $Os_{13}@Pt_{42}$.

Results

Energetics of adsorption

The overall reaction of the ORR reads $1/2O_2 + 2(H^+ + e^-) \Rightarrow H_2O$.[1] This reaction is described by the following sequential steps:

$$* + 1/2O_2 \Rightarrow *O, \quad (3)$$

$$*O + (H^+ + e^-) \Rightarrow *OH, \quad (4)$$

and

$$*OH + (H^+ + e^-) \Rightarrow H_2O, \quad (5)$$

where * denotes an adsorption site on the surface. First, a single O atom being elicited from an O_2 molecule is adsorbed on the adsorption site (*), which is referred to as a dissociation process [see Eq. (3)]. Following are subsequent hydrogenation steps that encompass electron transferring from the hydrogen atoms [see Eqs. (4) and (5)]. There exist only two reaction intermediates – O and OH adsorbates (*O and *OH, respectively) whose energetic significantly matters in the ORR.

To begin, it is of great importance to find energetically favourable adsorption sites on the surface of a NP. To do so, all available adsorption sites on the surface of 42 Pt atoms for all 12 combinations were examined; as a consequence, four possible reaction pathways were found, which involve a hollow site on a (111) facet and irregular sites, i.e. edge and vertex (Figure 1c). These pathways are illustrated in Figure 1c and so is the optimized intermediate at each configuration. Each of 13 core-shell combinations (plus Pt NP) takes its preferred reaction pathway(s) on these four types. The preferred pathways are listed in Table 1. Type I (Figure 1c) elucidates an ORR occurring on a single active site, i.e. a bridge site on an edge: O adsorption (*O) on the bridge site, and subsequent hydrogenation (*OH) on the same site. Type II – IV, however, refer to a sequential ORR involving different active sites for each step as illustrated in Figure 1c.

Interestingly, not all hollow sites on a (111) facet for Type III or IV take part in the reaction pathway. For instance, the hollow site indicated by the symbol (×) in Figure 1c does not offer a similar energetically favourable reaction pathway insomuch as the site is not the nearest hollow to any vertex. Provided these various ORR pathways that cannot occur in the slab model, a disparity between the CSNP and slab models is already seen. For slab bilayer catalysts, the hollow site on a (111) facet is understood to be mostly involved in the O adsorption.[2] In addition, the binding energy largely differs for the CSNP and slab models[2,21,25,37]. We will revisit what underlies this disparity in energy later in a following section. The calculations revealed that all CSNPs but $Ag_{13}@Pt_{42}$, $Fe_{13}@Pt_{42}$, and $Au_{13}@Pt_{42}$ prefer a bridge site for *O and thus Type I or II pathway (see Table 1). Notably, Type III and/or IV

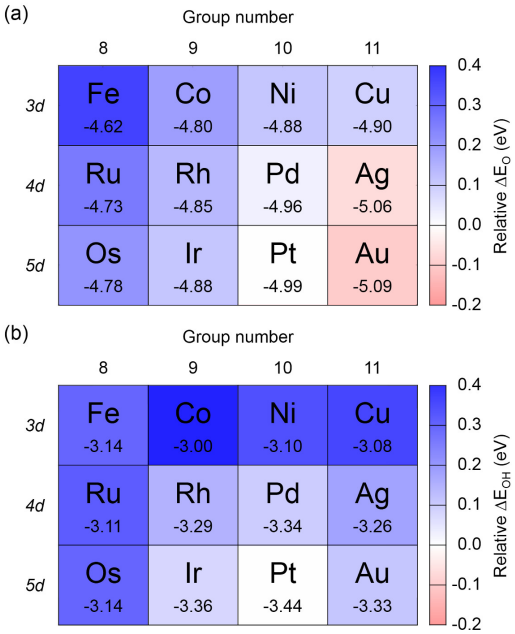

Fig. 2 Calculated adsorption energies of (a) O and (b) OH on the CSNPs with various cores in the periodic table.

pathway are likely seen in $Ag_{13}@Pt_{42}$, $Fe_{13}@Pt_{42}$ and $Au_{13}@Pt_{42}$. These CSNPs do not clearly discriminate between the bridge and hollow sites as the sites are energetically equivalent as seen in Table 1.

To estimate the catalytic activity, the adsorption energies of O and OH adsorbates (ΔE_O and ΔE_{OH}, respectively) on the CSNP surface were then evaluated; the results are shown on the periodic table (number on each core kind) in Figures 2a and b, respectively. Note that the colour bar indicates a deviation from the adsorption energy of each adsorbate on the Pt_{55} NP (equivalent to $Pt_{13}@Pt_{42}$), so that the value is termed as relative ΔE_O. By and large, the lower the group and period numbers, the higher the adsorption energies are, that is, the binding tends to be loose with the decrease of group and period numbers. In Figure 2a, this tendency is evident for O adsorption. The same is seen in several DFT studies on Pt-based bilayer slab models[2,15,25] albeit different in detail. A comparison in detail will be given later. However, OH adsorption exhibits some exceptional cases, in particular, $Ag_{13}@Pt_{42}$ and $Au_{13}@Pt_{42}$.

Thermodynamics of ORRs on various CSNP surfaces

For the time being, the catalytic activity of the CSNP needs to be described in terms of free energy (G), which is more straightforward in electrochemical reactions. To do so, the free energy diagram (free energy with respect to reaction coordinate) for 11 CSNPs plus Pt_{55} was acquired through the evaluation of the free energy at each step that involves each of the intermediates, viz. *O, *OH, and H_2O. Four reaction coordinates were under evaluation: $2(H^+ + e^-) + 1/2O_2$ (Coordinate 1), $2(H^+ + e^-)$ + *O (Coordinate 2), $(H^+ + e^-)$ + *OH (Coordinate 3), and H_2O (Coordinate 4). Accordingly, two reactions between sequential coordinates were defined as Eq. (4) (Reaction 1) and Eq. (5) (Reaction 2). In the calculation, the model system was subject to equilibrium, i.e. reversible dissociation, by assigning an electrostatic potential (U) of 1.23 V to the cathodic electrons (U_0 = 1.23 V), which corresponds to the ideal open-circuit voltage of the full-cell, relative to the standard hydrogen electrode. In addition, the anodic reaction $H_2 \Leftrightarrow 2(H^+ + e^-)$, was set to be reversible.

The calculated diagrams are plotted in Figure 3. For all cases, the free energy at Coordinate 2 is the minimum. The free energy at each coordinate takes after the previously calculated adsorption energy, so that the free energy likewise tends to increase with the decrease of group and period numbers as seen in Figure 2. The higher the free energy, the lower the energy barrier to overcome in order to reach the final coordinate (Coordinate 4). As shown in Figure 3, all CSNPs with *O but $Ag_{13}@Pt_{42}$ and $Au_{13}@Pt_{42}$ are predicted to represent higher free energies than Pt_{55}, rendering it possible to exhibit lower barrier heights than Pt_{55}. This is consistent with O adsorption energy on Ag and Au shells as seen in Figure 2a. Note that all CSNPs with *OH exhibit higher free energies than Pt_{55}.

In Figure 4, the free energy diagrams in Figure 3 were readily re-plotted to clearly view a difference in barrier height between Reaction 1 and 2, in short, R1 and R2, respectively; the barrier height for R1 and R2 reads ΔG_{R1} and ΔG_{R2}, respectively. Such a comparison provides the information as to the rate determining step and overpotential.[1] It is known that the reaction with the higher barrier most likely determines the entire reaction rate as well as the overpotential.

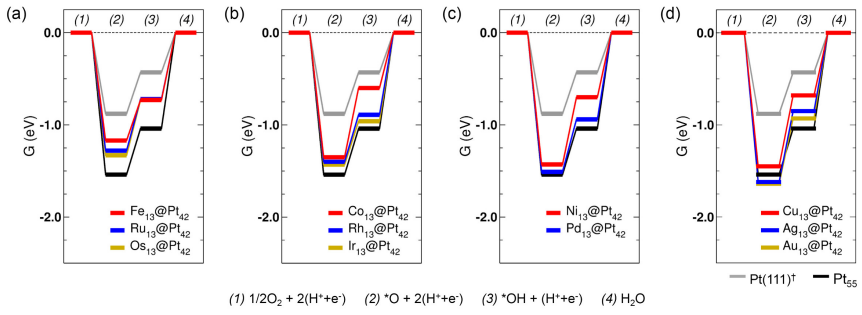

Fig. 3 Free energy diagram for the ORR on a given CSNP at the equilibrium potential (U=1.23 V). The red, blue, and yellow lines indicate the 3d, 4d, and 5d transition metal core, respectively. Note that the data for bulk Pt(111) were obtained from Ref. 1.

Nanoscale

PAPER

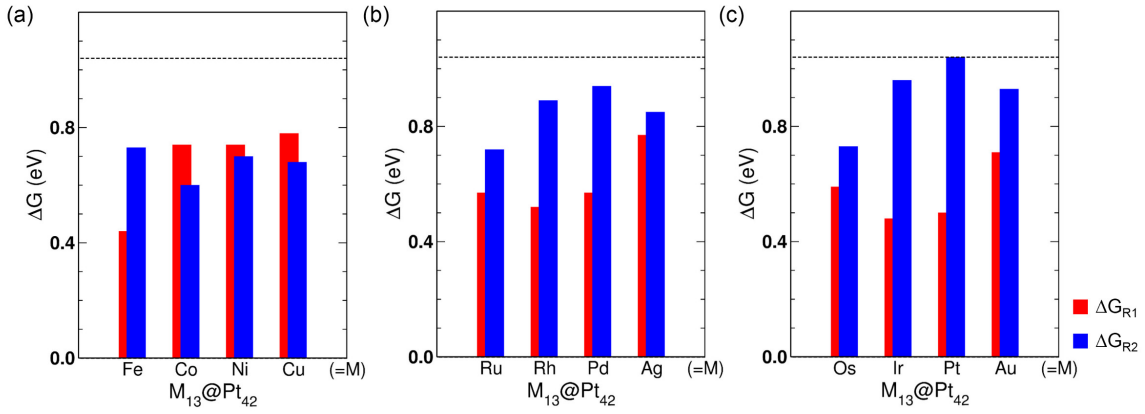

Fig. 4 Calculated free energy barriers for R1 and R2 (the sequential reactions in the overall ORR) at the equilibrium potential (U=1.23 V), which are on the CSNPs including (a) 3*d* (b) 4*d* and (c) 5*d* transition metal cores. ΔG_{R1} and ΔG_{R2} denote the free energy barriers for R1 and R2, respectively. The dot lines indicate the energy barrier of the rate-determining step (R2) of Pt_{55} for comparison.

In particular, overpotential η is likely determined, satisfying the following conditions:

$$G_{R1}(U) = G_{R1}(U_0) - e\eta \leq 0 \quad (7)$$

and

$$G_{R2}(U) = G_{R2}(U_0) - e\eta \leq 0, \quad (8)$$

where e denotes the elementary charge. Namely, satisfying these inequalities, both R1 and R2 do not encounter any energy barriers, so that no thermal activation is required. The minimal overpotential is thus $\max\{\Delta G_{R1}, \Delta G_{R2}\}/e$, $\eta = \Delta G_{max}/e$, so that the open-circuit voltage declines by the same amount as the overpotential. For instance, Pt_{55} represents ΔG_{R1} and ΔG_{R2} of 0.50 and 1.04 eV, respectively, (see Table 2). R2, therefore, determines the oxygen dissociation rate as a whole, resulting in a theoretical overpotential of 1.04 eV. $Co_{13}@Pt_{42}$, $Ni_{13}@Pt_{42}$ and $Cu_{13}@Pt_{42}$, however, fall into the case of R1–limited oxygen reduction, i.e. the rate of hydrogenation of *O limits the entire ORR. For the rest of the CSNPs, R2 plays a key role in limiting the entire ORR rate. ΔG_{R1} and ΔG_{R2} for all CSNPs and Pt_{55} are listed in Table 2.

As seen in Figure 4 and Table 2, all CSNPs feature a reduction in the rate-determining ΔG compared with Pt_{55}, giving rise to a reduction in the overpotential, e.g. approximately 31 percent (ca. 0.32 V) for $Ru_{13}@Pt_{42}$. This reduction is caused by the aforementioned decline in adsorption energy of O and OH. Overpotential is the most representative descriptor for ORR activity, enabling quantitative and straightforward comparisons between different CSNPs without invoking other quantities such as ΔE_O and ΔE_{OH}. ΔE_O, ΔE_{OH} and the corresponding overpotential η for all CSNPs are mapped onto an overpotential contour plot with ΔE_O and ΔE_{OH} shown in Figure 5. The lighter the colour bar, the lower the overpotential, and thus the higher the open-circuit voltage becomes. The results directly point that the use of a light metal core (lower period and group) places it at an advantage of lower overpotential. In comparison to the Pt_{55} NP in Figure 5, predicted is such that all CSNPs in our study represent good catalytic activity for ORR. Especially, CSNPs with 3*d* transition metal cores highlight the enhancement of catalytic activity, being in agreement with experimental results.[5,38-43]

Table 2 Calculated change in free energy upon each reaction – R1 and R2. The grey-filling denotes the smaller free energy change, indicating the rate-determining step.

CSNP	ΔG_{R1} (eV)	ΔG_{R2} (eV)	CSNP	ΔG_{R1} (eV)	ΔG_{R2} (eV)
$Fe_{13}@Pt_{42}$	0.44	0.73	$Pd_{13}@Pt_{42}$	0.57	0.94
$Co_{13}@Pt_{42}$	0.74	0.60	$Ag_{13}@Pt_{42}$	0.77	0.85
$Ni_{13}@Pt_{42}$	0.74	0.70	$Os_{13}@Pt_{42}$	0.59	0.73
$Cu_{13}@Pt_{42}$	0.78	0.68	$Ir_{13}@Pt_{42}$	0.48	0.96
$Ru_{13}@Pt_{42}$	0.57	0.72	Pt_{55}	0.50	1.04
$Rh_{13}@Pt_{42}$	0.52	0.89	$Au_{13}@Pt_{42}$	0.71	0.93

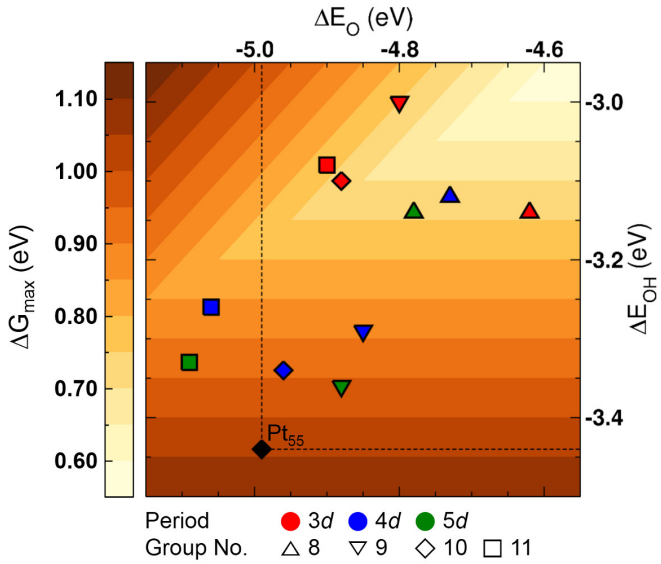

Fig. 5 Overpotential contour map with respect to O and OH adsorption energies.

Altering the core metal therefore serves as a workaround solution to the issues raised in Introduction.

Discussion

Origin of the different adsorption energies

Now, what follows is the understanding of the core metal-depending adsorption energy from microstructural and electronic structural perspectives. First, let us address the microstructural origin. A microstructural mismatch between the core and shell in a CSNP is inevitable in light of, for instance, different lattice parameters. It is thus evident that strain evolves in the CSNP, which most likely alters the electronic structure of surface Pt. Such a change in electronic structure upon strain has been theoretically predicted and so has the consequent change in adsorption energy. Also, the strain evolution in the CSNP appears different from that in catalytic bilayer catalysts given the additional geometric strain. Therefore, looking into the strain evolution and the resulting adsorption energy change matters in gaining an understanding of the catalytic activity.

A difference in diameter between a CSNP and a Pt_{55} NP (reference) was taken as a measure of the relative strain in the CSNP. The diameter was obtained by measuring the distance between two diagonal vertex atoms. Thus, a negative difference in diameter indicates compressive strain – relative to Pt_{55} – and the positive one tensile strain. For the (100) slabs, the lattice parameter, parallel to the surface, e.g. along [010] and [001], was taken for relative strain evaluation. Figure 6 shows the evaluated relative strain for all CSNPs in association with the previously calculated adsorption energy. Notably, the period 3 core metals impose compressive strain on surface Pt, whereas the strain distribution for periods 4 and 5 metals is rather widespread over both compressive and tensile regimes. Ag and Au core metals particularly cause tensile strain on surface Pt. The strain evaluation reveals the fact that the elements in each period are generally sorted by atomic number, e.g. Rh < Pd < Ag in period 4. This is attributed to the difference in lattice parameter between the core and the shell.

Considering the strain effect on the adsorption ener- shown in Figure 6 is such that the adsorption energy for both O and OH tends to decrease with respect to strain, being in decen- agreement with linearity. As a whole, given the regression line with a negative slope, a larger compressive strain is preferred s- as to enlarge the adsorption energy. Thus, the use of a ligh- metal core (lower period and group) is perhaps beneficial t- achieving a higher catalytic activity. The same is seen in OH adsorption energy in Figure 6b except $Ag_{13}@Pt_{42}$ an- $Au_{13}@Pt_{42}$. The liner fitting, however, features data deviation from the linear regression line; in particular, a large difference in O adsorption energy (ca. 0.28 eV) between $Fe_{13}@Pt_{42}$ an- $Cu_{13}@Pt_{42}$ in spite of their comparable strains. The deviatio- perhaps arises from other factors that are simultaneousl- involved in the adsorption energy in conjunction with – or dominant over – the strain effect.

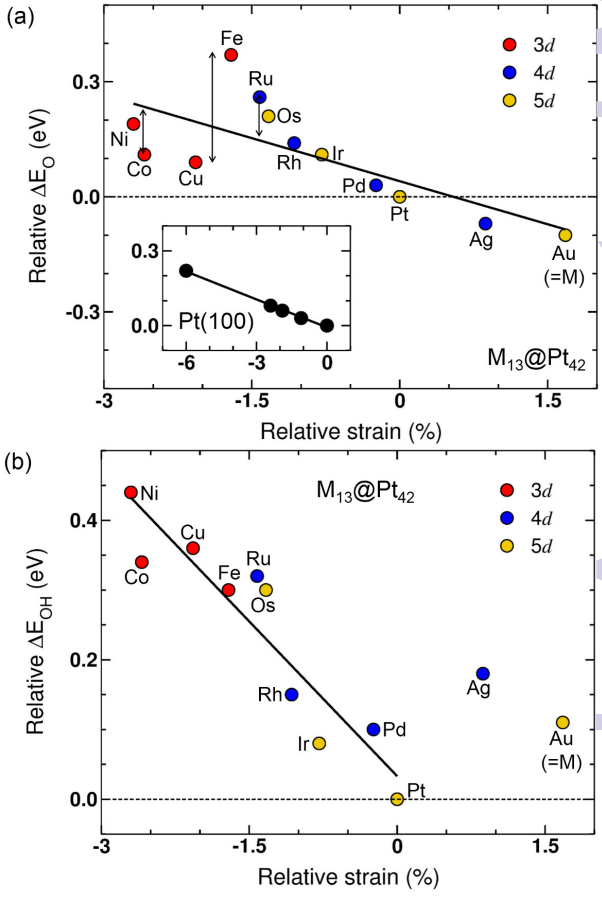

Fig. 6 Change in (a) O and (b) OH adsorption energy upon the strain bein- imposed on the CSNP due to the foreign core metal. The inset of (a) shows t- same data on the Pt(100) slab models as a control experimental. The strain was evaluated relative to the size of the Pt_{55} NP, and thus it was termed as 'relati- strain'. Likewise, the adsorption energy was evaluated relative to that of the Pt- NP. Several CSNPs are not well consistent with the regression lines; CSNPs with a deviation larger than 0.1 eV are highlighted with arrows.

Nanoscale

PAPER

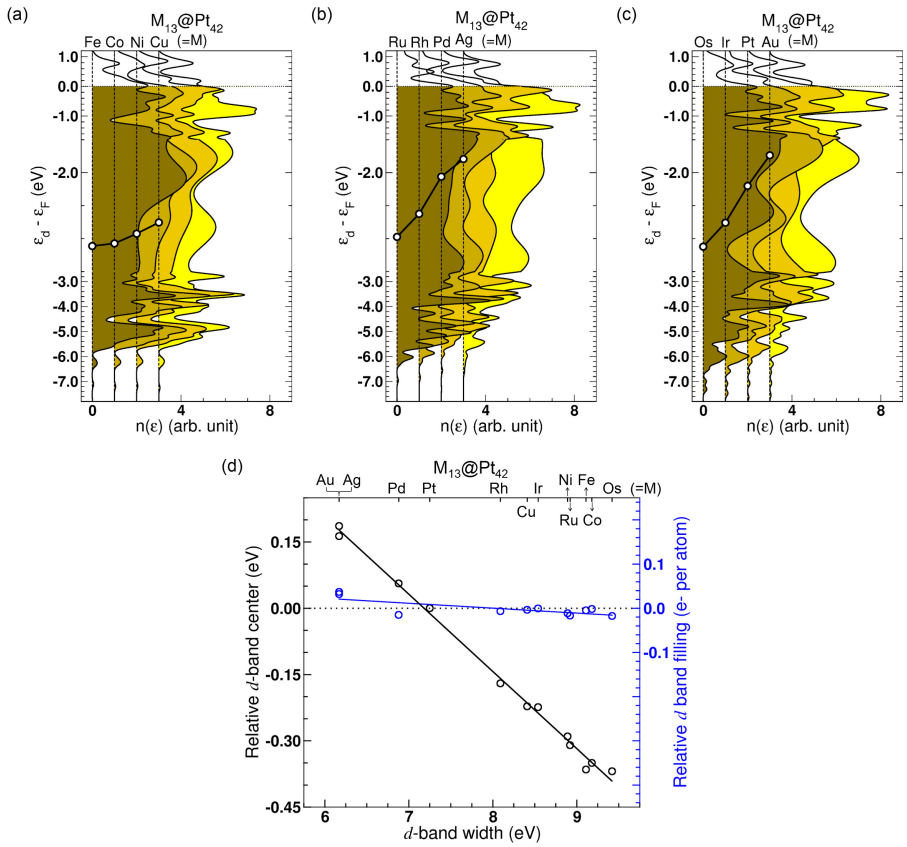

Fig. 7 Projected density of states (PDOS) and *d*-band properties. The open circles connected by the black solid line in (a) – (c) designate the *d*-band centers. Th relative *d*-band center and filling for all CSNPs are plotted in (d). These quantities are described related to Pt_{55}.

To confirm it, a control calculation on a preferentially (100)-oriented Pt film was conducted with respect to strain on the film. The O adsorption energy at a bridge site on the relaxed Pt(100) plane was under evaluation at various compressive strains. The results are shown in the inset of Figure 6a, representing a perfectly linear decrease in O adsorption energy with strain, serving as indirect evidence for the contribution of other effects than strain to the adsorption energy on the CSNP.

It is believed that the chemical effect – arising from the use of different cores – should also be taken into account, which is often referred to as the ligand effect.[14] The ligand effect explains the change of 5*d*-band of surface Pt upon the core metal, and the consequent alternation of the adsorption energy of adsorbates.[14] Taking the center of 5*d*-band as a representative of density of states (DOS) distribution over energy enables a quantitative description of the antibonding states with respect to the 5*d*-band center. Dragging down the 5*d*-band by using a proper core metal lets the antibonding states move down towards the Fermi level, filling the states with electrons. Thus, the binding of adsorbates to the surface tends to be loose. This mechanism is referred to as the *d*-band model.[17] Thus, the 5*d*-band center is taken as a descriptor for the rule of thumb estimation of adsorption energy. In order fo this effect to be justified, the 5*d*-band structure of surface Pt a each CSNP was evaluated. The calculated partial DOS (PDOS) as well as the 5*d*-band center is shown in Figures 7a – c According to the rectangular band model, a shift in the *d*-band center is determined by *d*-band filling and its band-width.[17] A seen in Figure 7d, The *d*-band filling of the CSNPs remain almost unchanged upon the core metal while the *d*-band width varies in the range 6.17 – 9.42 eV. As a result, the band cente largely varies upon the core metal.

Notably, within the same period, the use of a heavier co metal lifts up the band center and this holds for all three periods (see Figures 7a – c). The same tendency has been reported o Pt-based bilayer catalysts,[15,44] the feature in detail remarkably differs from that shown in our CSNPs though. Similar to th strain effect, light core metals are in general favourable so as to realize loose binding of adsorbates to the surface, and thus high catalytic activity. Namely, the *d*-band model[17] may successfu

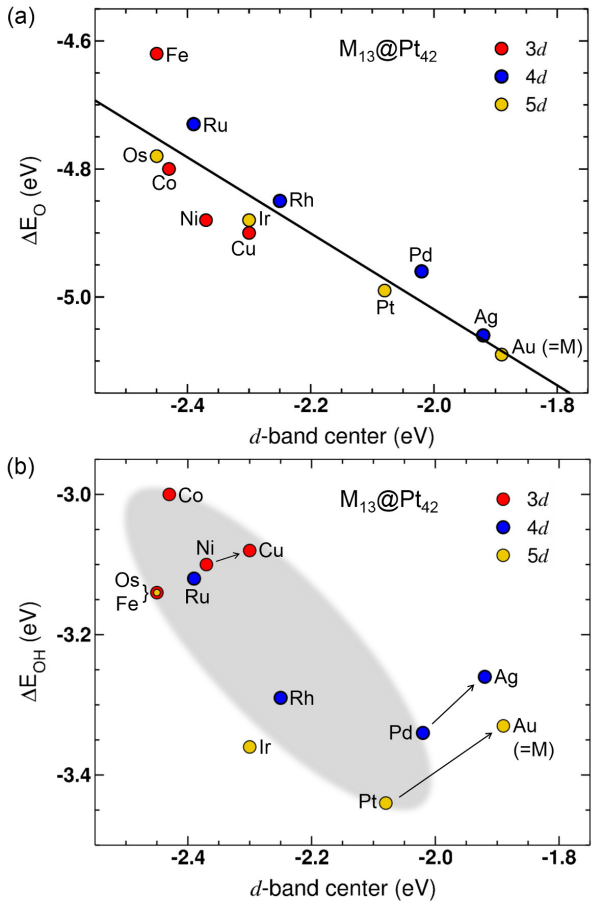

Fig. 8 General agreement of (a) O and (b) OH adsorption energy variation with the d-band model.

be applied to both O and OH adsorption energies. This behaviour is clearly seen in a relationship between the O adsorption energy and the *d*-band center as plotted in Figure 8a. However, when it comes to OH adsorption, the relation is rather weak and represents distribution albeit linear as a whole (see Figure 8b). Several core metals such as Cu, Ag, and Au are obvious exceptions; the increase in the *d*-band center rather increases the OH adsorption energy, enabling loose binding. Similar exceptions to the *d*-band model have been seen in recent DFT studies on OH adsorption on catalytic slabs by Xin and Linic.[45] The repulsive interaction between the adsorbate and the *d*-states – stemming from the large bond length between them, which is attributed to large electron density around O in OH – largely contributes to the adsorption energy. Consequently, the higher the *d*-band center, the more likely the one-electron energy in the binding configuration is larger.[45] Thus, the binding strength by and large tends to decline with atomic number in a period. In spite of these exceptions, our CSNP models generally follow the *d*-band model. This behaviour highlights distinguishable characteristics of the CSNP from the slab model.

Prediction of size effect

The effect of CSNP size on catalytic activity is of significant concern as the catalytic reaction most likely varies upon the size. Computational difficulties in altering CSNP size, i.e. the number of atoms, in a wide range are main obstacles to looking close at the size effect. Instead, we take two extremes – a CSNP (1 nm in diameter) and the Pt-based bilayer catalyst that likely represents the feature of a large size CSNP (> ca. 67 nm) – and predict the size effect. The bilayer relates the same atomic number in the sub-surface as the surface layer. Provided that, for a COh, the atomic ratio of the sub-surface to the surface layer remains below 99% until a diameter of ca. 6 nm, the bilayer catalyst perhaps represents a CSNP larger than 67 nm. In Figure 9, the O adsorption energies in Figure 8a are re-plotted with respect to the change of the *d*-band center relative to that of Pt_{55} in conjunction with the corresponding data for two bilayer catalysts, Pt/Cu(111) and Pt/Au(111). Note that for the bilayer catalysts the relative *d*-band center was measured from that of Pt(111). It is evident that incorporating a foreign core element in the CSNP evokes a small change in the *d*-band center compared with the cases of bilayer catalysts. The larger change for the bilayer catalysts is understood in terms of atomic ratio of foreign element to Pt – in the surface and sub-surface layers – that are considered to directly take part in the adsorption: 28 percent for the CSNP and 100 percent for the bilayer catalysts. Thus, the effect of subsurface substitution is supposed to be smaller on the CSNPs than the bilayer catalysts.

This rule of thumb understanding appears to hold for the corresponding change in ΔE_O as well. As mentioned earlier, the trends shown in Figure 2 are also seen in the corresponding bilayer catalysts[15]; however, the change in ΔE_O in detail is different as shown in Figure 9. Notably, a comparison between $Cu_{13}@Pt_{42}$ and Pt/Cu(111) highlights a possible strong size effect on the O adsorption energy; the size of a Cu@Pt CSNP determines the adsorption energy between these two poles far apart. The optimum point in ΔE_O can thus be determined regarding the adsorption energy and the cost and the dimension is optimized accordingly.

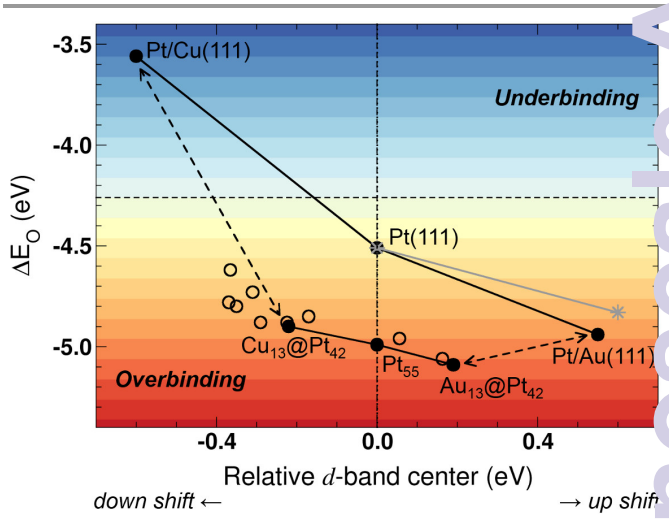

Fig. 9 Disparity in O adsorption energy and relative *d*-band center between our CSNP and bilayer slab models. The d-band center for the CSNPs and bilayer catalysts, Pt/M(111), was written relative to that of Pt_{55} and Pt(111), respectively. The gray-coloured asterisk denotes the O adsorption energy on

Pt/Au(111), which was taken from Ref. 25, for comparison. The open-circles denote the data for the other CSNPs.

Conclusions

In summary, we theoretically investigated ORR pathways on the surface of a CSNP – 55 atoms in total – with a Pt-shell (42 atoms) and a non-Pt-core (13 atoms) in an attempt to enhance the catalytic activity of the Pt_{55} NP. The core elements in use were 3 – 5*d* transition metals within group 8 – 11. Given that the ORR generally involves two distinctive adsorption intermediates, *O and *OH, we placed emphasis on the energetics involving these adsorbates on the CSNPs. We eventually evaluated the overpotential – open-circuit voltage-determining factor – for each CSNP combination and compared amongst them. The calculation results by and large revealed the advantage of use of a light metal core (lower period and group) in a CSNP in light of its low *O and *OH binding energies, and thus low overpotential. Irrespective of core elements, all 11 CSNPs showed better catalytic activities than Pt_{55}. The results are of importance in accelerating the practical and economical use of CSNP catalysts. In addition, the CSNP model systems in use in this study may fill the gap between experiment and theory by minimizing the disparity between them. In fact, our CSNP model systems are distinguished from slab ones by result in detail. Furthermore, the prediction of possible size effect – extrapolation from two extremes – highlights the possibility of size-mediated fine-tuning of the overpotential, so that it further underpins the significance of our results from a practical perspective.

We made an attempt to gain an understanding of the revealed trends in adsorption energy by invoking the strain and the ligand effect[15]. This attempt is worth being made from a scientific perspective; mainly, for justifying the *d*-band model – rule of thumb, but good, estimation of catalytic activity – in our CSNPs. To identify the strain effect, relative strain on each CSNP was evaluated and viewed in association with the corresponding *O and *OH adsorption energies. The shown data scattering most likely pointed to other effect, e.g. the ligand effect. The analysis of the adsorption energy for each CSNP with the corresponding *d*-band center verified the ligand effect, which perhaps changes the adsorption energy in conjunction with the aforementioned strain effect. Notably, both trends in the *O and *OH change upon *d*-band center are considered to obey the *d*-band model as a whole, some obvious exceptions to the general model are in sight, in particular, for the case of OH adsorption though. The exceptions appear attributed to the repulsive interaction between the high electron density in the O atom in OH and the high 5*d* electron density in the surface Pt layer – owing to the high electron density of the subsurface layer.

Acknowledgements

This research was mainly supported by the Nano Material Technology Development Program through the National Research Foundation of Korea (NRF) funded by the Ministry of Science, ICT and Future Planning (NRF-2009-0082471), and KIST grant (grant no. 2E25670). P.-R.C acknowledges financial support by Basic Science Research Program through the NRF funded by the Ministry of Education (2009-0093814). This work was also supported by the Supercomputing Center at the Korea Institute of Science and Technology Information with supercomputing resources including technical support (KSC-2013-C2-019).

References

1 J. K. Norskov, J. Rossmeisl, A. Logadottir, L. Lindqvist, J. R. Kitchin, T. Bligaard and H. Jonsson, *J. Phys. Chem. B*, 2004, **108**, 17886-17892.
2 Z. Duan and G. Wang, *Phys. Chem. Chem. Phys.*, 2011, **13**, 20178.
3 S. H. Noh, M. H. Seo, J. K. Seo, P. Fischer and B. Han, *Nanoscale*, 2013, **5**, 8625-8633.
4 K. Shin, D. H. Kim and H. M. Lee, *ChemSusChem*, 2013, **6**, 1044-1049.
5 P. Strasser, S. Koh, T. Anniyev, J. Greeley, K. More, C. Yu, Z. Liu, S. Kaya, D. Nordlund, H. Ogasawara, M. F. Toney and A. Nilsson, *Nat. Chem.*, 2010, **2**, 454-460.
6 C. Wang, N. M. Markovic and V. R. Stamenkovic, *ACS Catal.*, 2012, **2**, 891-898.
7 G. Wang, H. Wu, D. Wexler, H. Liu and O. Savadogo, *J. Alloys Compd.*, 2010, **503**, L1-L4.
8 B. C. Han, C. R. Miranda and G. Ceder, *Phys. Rev. B*, 2008, **77**, 075410.
9 D. H. Lim and J. Wilcox, *J. Phys. Chem. C*, 2012, **116**, 3653-3660.
10 B. Han, V. Viswanathan and H. Pitsch, *J. Phys. Chem. C*, 2012, **116**, 6174-6183.
11 K. J. J. Mayrhofer, B. B. Blizanac, M. Arenz, V. R. Stamenkovic, P. N. Ross and N. M. Markovic, *J. Phys. Chem. B*, 2005, **109**, 14433-14440.
12 J. Rossmeisl, G. S. Karlberg, T. Jaramillo and J. K. Norskov, *Faraday Discuss.*, 2008, **140**, 337-346.
13 J. Shin, J. H. Choi, Y. S. Bae and S. C. Lee, *Chem. Phys. Lett.*, 2014, **610-611**, 86-90.
14 Y. Gauthier, M. Schmid, S. Padovani, E. Lundgren, V. Bus, G. Kresse, J. Redinger and P. Varga, *Phys. Rev. let.*, 2001, **87**, 036103.
15 J. R. Kitchin, J. K. Norskov, M. A. Barteau and J. G. Chen, *J. Chem. Phys.*, 2004, **120**, 10240-10246.
16 M. Mavrikakis, B. Hammer and J. K. Norskov, *Phys. Rev. Lett.*, 1998, **81**, 2819-2822.
17 B. Hammer and J. K. Norskov, *Adv. Catal.*, 2000, **45**, 71-129.
18 W. Tang and G. Henkelman, *J. Chem. Phys.*, 2009, **130**, 194504.
19 B. B. Xiao, Y. F. Zhu, X. Y. Lang, Z. Wen and Q. Jiang, *Sci. Rep.*, 2014, **4**, 5205.
20 H. C. Tsai, Y. C. Hsieh, T. H. Yu, Y. J. Lee, Y. H. Wu, B. V. Merinov, P. W. Wu, S. Y. Chen, R. R. Adzic and W. A. Goddard III, *ACS Catal.*, 2015, **5**, 1568-1580.
21 L. Yang, M. B. Vukmirovic, D. Su, K. Sasaki, J. A. Herron, M. Mavrikakis, S. Liao and R. R. Adzic, *J. Phys. Chem. C*, 2013, **117**, 1748-1753.
22 J. X. Wang, H. Inada, L. Wu, Y. Zhu, Y. M. Choi, P. Liu, W. P. Zhou and R. R. Adzic, *J. Am. Chem. Soc.*, 2009, **131**, 17298-17302.

23 S. Guo, X. Zhang, W. Zhu, K. He, D. Su, A. Mendoza-Garcia, S. F. Ho, G. Lu and S. Sun, *J. Am. Chem. Soc.*, 2014, **136**, 15026-15033.
24 J. Greeley and M. Mavrikakis, *Nat. Mater.*, 2004, **3**, 810-815.
25 A. U. Nilekar and M. Mavrikakis, *Surf. Sci.*, 2008, **602**, L89-L94.
26 J. K. Nørskov, T. Bligaard, A. Logadottir, J. R. Kitchin, J. G. Chen, S. Pandelov and U. Stimming, *J. Electrochem. Soc.*, 2005, **152**, J23.
27 J. K. Norskov, T. Bligaard, J. Rossmeisl and C. H. Christensen, *Nat. Chem.*, 2009, **1**, 37-46.
28 P. W. Atkins, *Physical Chemistry*, Oxford University Press, New York, 6th edn., 1998, pp. 485, 925-927, 942.
29 S. Kandoi, A. A. Gokhale, L. C. Grabow, J. A. Dumesic and M. Mavrikakis, *Catal. Lett.*, 2004, **93**, 93-100.
30 R. C. Weast, *CRC Handbook of Chemistry and Physics*, CRC Press, Boca Raton, 49th edn., 1968-1969, pp. D109.
31 J. P. Perdew, K. Burke and M. Ernzerhof, *Phys. Rev. Lett.*, 1966, **77**, 3865-3868.
32 V. Blum, R. Gehrke, F. Hanke, P. Havu, V. Havu, X. Ren, K. Reuter and M. Scheffler, *Comput. Phys. Commun.*, 2009, **180**, 2175-2196.
33 V. Havu, V. Blum, P. Havu and M. Scheffler, *J. Comput. Phys.*, 2009, **228**, 8367-8379.
34 E. V. Lenthe, E. J. Baerends and J. G. Snijders, *J. Chem. Phys.*, 1994, **101**, 9783-9792.
35 R. Feynman, *Phys. Rev.*, 1939, **56**, 340-343.
36 H. Hellmann, *Z. Phys.*, 1933, **85**, 180-190.
37 S. Alayoglu, A. U. Nilekar, M. Mavrikakis and B. Eichhorn, *Nat. Mater.*, 2008, **7**, 333-338.
38 G. Gupta, D. A. Slanac, P. Kumar, J. D. Wiggins-Camacho, X. Wang, S. Swinnea, K. L. More, S. Dai, K. J. Stevenson and K. P. Johnston, *Chem. Mater.,* 2009, **21**, 4515-4526.
39 J. G. Oh, H. S. Oh, W. H. Lee and H. Kim, *J. Mater. Chem.*, 2012, **22**, 15215.
40 L. Gan, M. Heggen, S. Rudi and P. Strasser, *Nano lett.*, 2012, **12**, 5423-5430.
41 C. Wang, M. Chi, G. Wang, D. V. D. Vliet, D. Li, K More, H. H. Wang, J. A. Schlueter, N. M. Markovic and V. R. Stamenkovic, *Adv. Funct. Mater.*, 2011, **21**, 147-152.
42 H. Yano, M. Kataoka, H. Yamashita, H. Uchida and M. Watanabe, *Langmuir*, 2007, 23, (11), 6438-6445.
43 C. Wang, D. V. D. Vilet, K. C. Chang, H. D. You, D. Strmcnik, J. A. Schlueter, N. M. Markovic and V. R. Stamenkovic, *J. Phys. Chem. C.*, 2009, 113, (45), 19365-19368.
44 A. Ruban, B. Hammer, P. Stoltze, H. L. Skriver and J. K. Norskov, *J. Mol. Catal. A*, 1997, **115**, 421-429.
45 H. Xin and S. Linic, *J. Chem. Phys.*, 2010, **132**, 221101.